Accepted in IEEE Transactions on Antennas and Propagation, vol. 72, no. 1, pp. 791-799, Jan. 2024, doi: 10.1109/TAP.2023.3327776

Analysis and Improvement of the Stability of a 3D FDTD Subgridding Method by Applying a LECT-based Technique

Antonio J. Martín Valverde, Miguel Ruiz-Cabello N., Amelia Rubio Bretones, Alberto Gascón Bravo, Salvador Gonzalez García *IEEE, Senior Member*

***Abstract*—This paper studies and improves the stability of a Finite Difference Time Domain (FDTD) subgridding method based on the orthogonalized integral-based methodology. First, we identify the electric and magnetic field components of the FDTD lattices used at the interface between different mesh regions playing a critical role in its stability. Then, we employ them to find a closed criterion for the Courant-Friedrichs-Lewy Number (CFLN). Next, we analyze the stability by the classical spectral method and validate it with numerical heuristic simulations, proving the methodology used in the analytical approach. This information is used to devise a Locally Enlarged Cell Technique (LECT) to modify locally the scheme used to update the field components identified as most critical for stability so that an increased time step can be used. Finally, we analyze the effect of these modifications on the accuracy of the method for typical transmission and scattering problems.**

***Index Terms*—Finite-difference time-domain (FDTD), locally enlarged cell technique (LECT), numerical stability, spectral analysis, subgridding**

I. Introduction

Finite-Difference Time-Domain method [1], [2] is a widely used numerical scheme that provides an explicit expression to solve Maxwell's equations. It consists of a marching-on-in-time explicit scheme whose maximum time step for stability Δt_{max} is bounded by the minimum space step Δ_{min} through the well-known Courant-Friedrich-Lewy (CFL) criterion (quantified by the CFL number *CLFN*).

When FDTD is used for multiscale problems combining small geometrical features with larger ones, a gradual mesh technique can naturally be used [3], [4], smoothly adapting the space mesh between coarser and finer areas. However, the overall computer performance of this approach is degraded since the time step needs to be unnecessarily reduced in the overall space to meet the CFL criterion enforced by the finest space step.

Different subcell methods have been developed over the years for specific phenomena, overcoming that limitation by providing local equations for wires, slots, panels, etc., not degrading the overall FDTD scheme, and without requiring an explicit mesh refinement [5]–[8].

All the authors are with Department of Electromagnetism and Matter Physics, University of Granada, 18071 Granada. Spain.

The work described in this paper and the research leading to these results was supported by the Spanish MICINN EU FEDER Project PID2019.106120RB.C33, and by the Junta de Andalucia FEDER project B-TIC-700-UGR20

As an alternative, subgridding methods [9] provide a more general approach, just resorting to fine meshing at specific locations and keeping coarser meshes elsewhere. Subgridding methods combine cells of different sizes to suitably wrap the different parts of a problem with the appropriate mesh size for accuracy.

Typically, subgridding algorithms locally divide some Yee cells (material and field discontinuities) into finer ones where needed. Usually, an integer ratio (named *refinement ratio*) along every cartesian direction is used, leading to a set of regions of refined cells. In most subgridding algorithms, this division may be applied recursively, leading to more than two regions, here named *subgridding levels*. Cells within a subgridding level are treated as the usual Yee cells, and therefore the FDTD algorithm may be applied without further consideration. However, the Yee scheme cannot be applied at the boundaries between different subgridding levels for containing non-conforming degrees of freedom. Specific approaches exist to devise the connection algorithms [10]–[19] between subgridding levels. Furthermore, in these methods, it is desirable to maintain the CFLN at different subgrid levels for efficiency and reduction of the numerical dispersion. For this purpose, local time stepping (LTS) is required to advance each level with different time steps.

Due to this complexity, subgridding schemes may require implicit expressions, interpolations, and extrapolations (even without field reciprocity). These are often the cause of late-time instabilities [14], [20], [21], making stability analysis an essential topic in subgridding methods.

In previous a work [18], [19], we focus on the orthogonalized integral-based subgridding (OI-SG) algorithm based on the original work presented in [11], [12] and demonstrated its robustness with application to a canonical multiscale test case. All heuristic analyses of the OI-SG method have proved so far to be robustly stable. This method can be seen as a finite integration technique (FIT) [22], [23] applied to a specifically shaped main-dual grid in a subgridding boundary. Interestingly, the resulting algorithm provides an explicit expression that ensures field reciprocity. In [18], an LTS methodology was devised to maintain the overall stability region-by-region, showing heuristically that only an overall CFLN $= 0.65$ was required to yield stable results.

However, rigorously analyzing the stability of local schemes connecting different methods is challenging, and in some cases, stability is only supported by heuristic studies. Many

works have been published in recent years on the subject [24]–[30]. However, not all methods are trivially appliable to the OI-SG, mainly due to the complex nature of the level boundaries and the presence of LTS. In this work, we provide an analysis of the stability of the OI-SG method by identifying the local components having more impact on the CFLN reductions and propose a methodology to increase the overall CFLN limit further. We show that, even if the condition found by our approach appears to be more restrictive than the classical spectral one, corroborated by heuristic simulations, it can be used to improve the CFL. We profit from this fact in the second part of this work with this purpose.

Our methodology starts by identifying the boundary fields whose updating scheme has more impact on the method stability. Next, we use this information to propose a novel method, with no extra computational cost, inspired by the Locally Enlarged Cell Technique (LECT), initially devised for the conformal FDTD method [31], to locally modify the parameters used to update components, thus pushing away the upper CFLN limit. Finally, the impact of the LECT modifications is also assessed in accuracy with representative examples of transmission and scattering problems.

Though our analytical approach is conducted with OI-SG, the methodology can generally serve where connecting time-space schemes are needed to hybridize different methods.

This work is structured as follows. First, in section II, we describe the basics of the OI-SG algorithm that are necessary for the reader to understand the stability analysis. Second, in section III, we explain two approaches used to study the stability of the subgridding algorithm, supported by a heuristic analysis, and we expose the achieved results. Third, in section IV, we describe how LECT can be applied based on the previous section and show the stability improvement. Fourth, we show the effects of LECT in actual simulations in section V. Finally, we draw some conclusions in section VI.

II. Subgridding description

In this section, we revisit the basics of the OI-SG algorithm of [18]. For this, let us consider a simple FDTD lattice of an electric (main) grid and a magnetic (dual) one. Let us henceforth refer to the main grid cells simply as Yee cells.

Also, for simplicity, we assume that any Yee cell relevant to the explanation is embedded into a cubic lattice. That is, the space steps are the same in each Cartesian axis $\Delta x = \Delta y = \Delta z \equiv \Delta$. Now, to perform the subgridding process in a given Yee cell, we subdivide it by using a refinement ratio of r_x, r_y, and r_z in each Cartesian axis, respectively, leading to a number of cells $N_{\text{cells}} = r_x\, r_y\, r_z$. The OI-SG algorithm could be applied to any arbitrary positive integer value for r_x, r_y, and r_z. However, this work will take a constant refinement where $r_x = r_y = r_z \equiv r = 2$ (Fig. 1).

If we apply the cell subdivision to a given set of Yee cells, the overall simulation domain splits into two regions: the one formed by the coarse cells and the one formed by the fine ones. These regions are referred to as the level domains. This division may be applied recursively to the cells already subgridded, therefore obtaining more than two level domains. Each level domain is associated with a subgrid level n_{sg}, where the one associated with the finest cells is $n_{\text{sg}} = 0$, and each coarser subgrid level increases by one until we reach the coarsest level N_{sg}. The surface that lies between two levels is named the level boundary. This recursive refinement process leads to specific space-steps $\Delta_{n_{\text{sg}}} = 2^{n_{\text{sg}}}\Delta_0$ and time-steps $\Delta t_{n_{\text{sg}}}$ for any given level n_{sg}. Note that $\Delta t_{n_{\text{sg}}}$ may be constant for every level or depend proportionally on $\Delta_{n_{\text{sg}}}$, in which case we use the Local Time Stepping (LTS) strategy described in [18].

In order to complete the explanation of the spatial subgridding process, we must note two more facts. First, in each level boundary between two levels n_{sg} and $n_{\text{sg}} + 1$, for orthogonalization purposes [18], we shift the central vertex of every coarse cell face towards the subgridded region by a certain distance $\delta_{n_{\text{sg}}}$, as shown in Fig. 1d. The parameter $\delta_{n_{\text{sg}}}$ will always be defined to be proportional to $\Delta_{n_{\text{sg}}}$, and therefore the ratio $\delta_{\text{r}} \equiv \delta_{n_{\text{sg}}}/\Delta_{n_{\text{sg}}}$ is a constant in the entire simulation. Second, the dual grid can be trivially placed inside any subgridded region as in any usual FDTD lattice. However, that is not the case in the level boundaries, where the behavior of the dual grid is not trivial. We solve this issue by connecting all the dangling dual grid nodes in the fine grid to the closest node in the coarse grid.

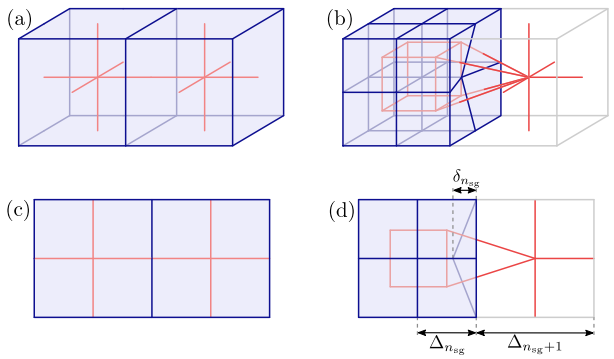

Fig. 1. Representation of Yee cells without subgridding (a), with subgridding (b), and their respective 2D projections (c,d). The magnetic grid is represented in red, whereas the other edges belong to the electric grid. In the subgridded figures (b,d), blue edges represent refined cells, and gray represents the non-refined ones.

The update equations can be easily obtained from this point by applying the FIT [22], [23]. Let us consider, for example, Ampere's Law without sources:

$$\frac{d}{dt}\int_S \vec{E}\cdot d\vec{S} = \frac{1}{\varepsilon}\oint_{\partial S}\vec{H}\cdot d\vec{l}. \tag{1}$$

We may approximate the surface and line integrals for a particular discrete electric component $\vec{E}_i$ embedded in its corresponding surface $S_{E,i}$ as follows:

$$\begin{aligned}\int_{S_{E,i}}\vec{E}\cdot d\vec{S} &\simeq E_i\int_{S_{E,i}}\hat{E}_i\cdot d\vec{S} = \tilde{S}_{E,i}\,E_i,\\ \oint_{\partial S_{E,i}}\vec{H}\cdot d\vec{l} &\simeq \sum_{\substack{j\\ H_j\,\in\,\mathcal{S}\{E_i\}}}\text{sgn}_{E,i,j}\,H_j\,l_{H,j},\end{aligned} \tag{2}$$

where $E_i = |\vec{E}_i|$, $\hat{E}_i = \vec{E}_i/E_i$, $\mathcal{S}\{E_i\}$ is the set of the magnetic field components that surround E_i, $l_{H,j}$ is the length of the grid edge corresponding to the magnetic field component H_j, and $\text{sgn}_{E,i,j} = \pm 1$ is positive if $\vec{H}_j$ is directed according to the field circulation used on $\partial S_{E,i}$ and negative otherwise. Also, we have defined the equivalent surface

$$\tilde{S}_{E,i} := \int_{S_{E,i}} \hat{E}_i \cdot d\vec{S}. \tag{3}$$

Note that the surface $S_{E,i}$ is not always planar, so the surface integral cannot be trivially written. However, for our subgridding scheme, (3) can always be assessed by breaking $S_{E,i}$ into one or more planar surfaces, therefore contributing with their surfaces multiplied by the cosine of the angle between their normal vector and $\hat{E}_i$. An example of this work's overall finite integration scheme is shown in Fig. 2.

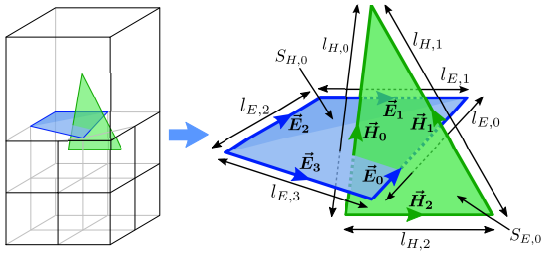

Fig. 2. An example of the finite integration scheme applied to the OI-SG field components. In this case, $\mathcal{S}\{E_0\} = \{H_0, H_1, H_2\}$ and $\mathcal{S}\{H_0\} = \{E_0, E_1, E_2, E_3\}$.

Finally, by substituting in (1) and applying finite differences in the time derivative, we obtain a general update equation for any field component E_i:

$$E_i|^{n+1} = E_i|^n + \frac{\Delta t}{\varepsilon \tilde{S}_{E,i}} \sum_{\substack{j \\ H_j \in \mathcal{S}\{E_i\}}} \text{sgn}_{E,i,j} l_{H,j} \; H_j|^{n+1/2}, \tag{4}$$

This process can be analogously applied to Faraday's Law in order to obtain the updated equation to the magnetic field,

$$H_i|^{n+1/2} = H_i|^{n-1/2} - \frac{\Delta t}{\mu \tilde{S}_{H,i}} \sum_{\substack{j \\ E_j \in \mathcal{S}\{H_i\}}} \text{sgn}_{H,i,j} l_{E,j} \; E_j|^n, \tag{5}$$

We note that the usual FDTD update equations are a particular case of (4) and (5) where $\tilde{S}_{E,i} = \tilde{S}_{H,i} = \Delta^2$, $l_{E,i} = l_{H,i} = \Delta$ and the number of elements in $\mathcal{S}\{E_i\}$ and $\mathcal{S}\{H_i\}$ is always 4, which is not necessarily true in the OI-SG scheme.

Now, for a given level boundary between the levels n_{sg} and $n_{\text{sg}} + 1$, we define the equivalent surface ratio and the edge length ratio, respectively, as

$$\begin{aligned} \tilde{S}_{\text{r},U,i} &:= \tilde{S}_{U,i}/\Delta_{n_{\text{sg}}}^2, \\ l_{\text{r},U,i} &:= l_{U,i}/\Delta_{n_{\text{sg}}}, \end{aligned} \tag{6}$$

where U can be either E or H. This scheme classifies all the possible field components that the usual FDTD scheme cannot trivially update by their equivalent surfaces and edge lengths. This classification is shown in Fig. 3 and Tab. I.

TABLE I
FIELD TYPE CLASSIFICATION FOR BOUNDARY-LEVELS. IN EACH EXPRESSION, Δ REFERS TO THE CELL LENGTH OF THE FINER LEVEL IN THE BOUNDARY CONSIDERED. FIELD TYPES CORRESPOND TO FIG. 3.

Electric		
Type	$\tilde{S}_{\text{r},E}$	$l_{\text{r},E}$
1	$\frac{3+\delta_{\text{r}}}{4\sqrt{1+{\delta_{\text{r}}}^2}}\sqrt{1+{\delta_{\text{r}}}^2}$	
2	9/4	1
3	1	$1-\delta_{\text{r}}$
4	3	1
5	2	1
6	3/2	1

Magnetic		
Type	$\tilde{S}_{\text{r},H}$	$l_{\text{r},H}$
1	$\frac{3+\delta_{\text{r}}}{\sqrt{11}}$	$\frac{\sqrt{11}}{2}$
2	$1-\frac{\delta_{\text{r}}}{2}$	1
3	$1-\delta_{\text{r}}$	1
4	N/A	2

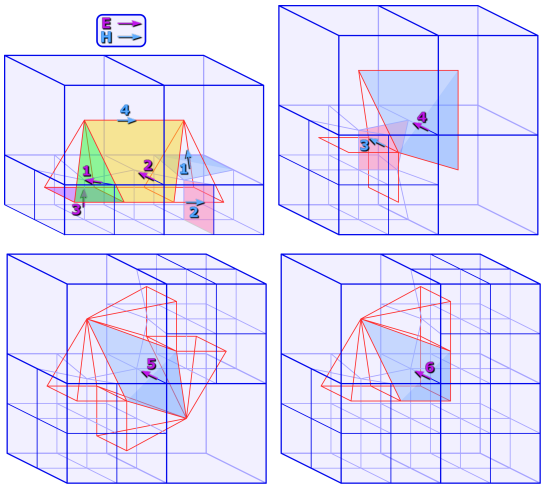

Fig. 3. Subgridding level boundary field types. Each field component type is classified, and their integration surfaces are represented. Field types correspond to Tab. I.

III. STABILITY ANALYSIS

Our goal in this section is to provide a study of the stability of this subgridding method based on how the paremeter δ_{r} affects the maximum stable $\Delta t_{n_{\text{sg}}}$. In a usual FDTD cubic method simulation, the CFL criterion would allow us to write

$$\Delta t = \text{CFLN}\frac{\Delta}{\sqrt{3}\,c_0}; \quad 0 < \text{CFLN} \leqslant 1, \tag{7}$$

As the introduction states, we are applying LTS and therefore $\Delta t_{n_{\text{sg}}} \propto \Delta_{n_{\text{sg}}}$. We can combine this with (7) in order to establish a global CFLN parameter for the whole simulation, where

$$\Delta t_{n_{\text{sg}}} = \text{CFLN}\frac{\Delta_{n_{\text{sg}}}}{\sqrt{3}\,c_0}. \tag{8}$$

Given this equation, the strategies described below to study the stability are designed to obtain the maximum stable CFLN as a function of δ_{r}. First, we have used an analytical method based on the partially filled cells criterion used in [32], [33], and, secondly, a classical spectral analysis of the evolution matrix. Finally, a heuristic method serves to corroborate the results of the latter.

A. Analytical expression

This methodology was justified in [18]. However, a different but equivalent approach is going to be presented here. This explanation is based, with slight changes, on the work presented in [32] that established a stability criterion on the partially filled cells in the conformal subcell method.

The expression in (7) may be written as

$$\Delta t \leqslant \frac{\Delta\sqrt{\varepsilon\mu}}{\sqrt{3}}. \tag{9}$$

We may now rewrite the update equation (4) as

$$\begin{aligned} E_i|^{n+1} &= E_i|^n + \sum_j \frac{\Delta t}{\left(\varepsilon \dfrac{\tilde{S}_{E,i}}{l_{H,j}\,\Delta}\right)\Delta}\; H_j|^{n+1/2} = \\ &= E_i|^n + \sum_j \frac{\Delta t}{\tilde{\varepsilon}_{i,j}\,\Delta}\; H_j|^{n+1/2}, \end{aligned} \tag{10}$$

where H_j are the fields E_i needs in order to update itself, and we have defined

$$\tilde{\varepsilon}_{i,j} := \varepsilon \frac{\tilde{S}_{E,i}}{l_{H,j}\,\Delta} = \varepsilon \frac{\tilde{S}_{\mathrm{r},E,i}}{l_{\mathrm{r},H,j}}. \tag{11}$$

We note that $\tilde{\varepsilon}$ acts as an equivalent electric permeability for the pair of field components (E_i, H_j). Analogously, we may obtain the equivalent magnetic permittivity $\tilde{\mu}$ from (5) and write it as

$$\tilde{\mu}_{i,j} := \mu \frac{\tilde{S}_{H,j}}{l_{E,i}\,\Delta} = \mu \frac{\tilde{S}_{\mathrm{r},H,j}}{l_{\mathrm{r},E,i}}. \tag{12}$$

Now, we insert these values in (9) and obtain the following expression:

$$\Delta t \leqslant \sqrt{\frac{\tilde{S}_{\mathrm{r},E,i}}{l_{\mathrm{r},E,i}} \frac{\tilde{S}_{\mathrm{r},H,j}}{l_{\mathrm{r},H,j}}}\, \frac{\Delta}{\sqrt{3}\,c}. \tag{13}$$

We note that this expression must be fulfilled by every field pair (E_i, H_j) that are neighbors, i.e., they use each other in their update equation. This, in combination with (7) yields to the final expression:

$$\mathrm{CFLN} \leqslant \min_{(E_i,H_j)\ \text{neighbors}} \sqrt{\frac{\tilde{S}_{\mathrm{r},E,i}}{l_{\mathrm{r},E,i}} \frac{\tilde{S}_{\mathrm{r},H,j}}{l_{\mathrm{r},H,j}}}. \tag{14}$$

Particularly, if we take all the possible neighboring field pairs (E_i, H_j) present in this subgridding scheme (Fig. 3 and Tab. I), we get the following explicit expression:

$$\mathrm{CFLN}_{\max}(\delta_\mathrm{r}) = \begin{cases} \text{Field types: E-1, H-1:} \\ \dfrac{3+\delta_\mathrm{r}}{\sqrt{22\left(1+{\delta_\mathrm{r}}^2\right)}} \quad \text{if} \quad \delta_\mathrm{r} \leqslant \dfrac{5}{13} \\ \\ \text{Field types: E-1, H-3:} \\ \sqrt{\dfrac{(3+\delta_\mathrm{r})\,(1-\delta_\mathrm{r})}{4\left(1+{\delta_\mathrm{r}}^2\right)}} \quad \text{if} \quad \delta_\mathrm{r} > \dfrac{5}{13} \end{cases} \tag{15}$$

This function is drawn in Fig. 4. Finally, it should be noted that this criterion (15) is not a rigorous stability condition and is only a guideline for what the stable CFLN could be.

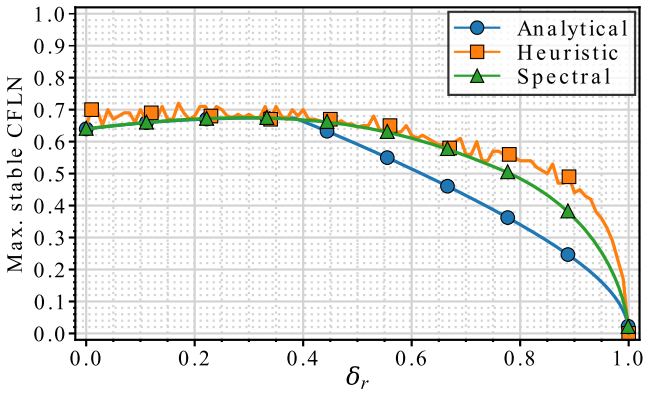

Fig. 4. Maximum stable CFLN value as a function of δ_r found by the spectral method, heuristically corroborated. The analytical criterion is shown in blue.

B. Spectral analysis

A classical method to analyze the stability of a given local time-invariant (LTI) algorithm is the spectral analysis of the numerical linear operator approaching the continuous one (assuming this to be passive). This idea has been used in many different previous works ([25], [34], to name a few) since the spectral radius is deeply related to exponential instabilities [25]. Generally speaking, an LTI algorithm may be written as follows:

$$\begin{aligned} f|^{n+1} &= A\, f|^n + S|^n, \\ f|^0 &= f_0, \end{aligned} \tag{16}$$

where $f|^n$ is the state at the instant $t = n\Delta t$, A is a constant linear operator that does not depend on the state, $S|^n$ are the sources at the instant $t = n\Delta t$, and f_0 is the initial condition state.

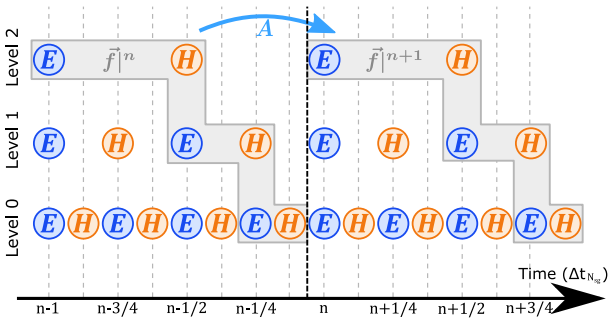

Fig. 5. Scheme of the time-stepping. Arrow represents a coarse time step, which may be considered a linear operator applied recursively over time.

The OI-SG algorithm with LTS can be written as a sequence of linear operators applied periodically, each of them being the update of a given subgrid level's electric or magnetic components. The composition of one period of these operators can be seen as one full update of a time-step $\Delta t_{N_{\mathrm{sg}}}$ (illustrated in Fig. 5), and constitutes a linear operator A that fulfills (16):

$$\begin{pmatrix} E|^{n}_{N_{\text{sg}}} \\ H|^{n+1/2}_{N_{\text{sg}}} \\ E|^{n+1/2}_{N_{\text{sg}}-1} \\ H|^{n+3/4}_{N_{\text{sg}}-1} \\ \vdots \end{pmatrix} = A \begin{pmatrix} E|^{n-1}_{N_{\text{sg}}} \\ H|^{n-1/2}_{N_{\text{sg}}} \\ E|^{n-1/2}_{N_{\text{sg}}-1} \\ H|^{n-1/4}_{N_{\text{sg}}-1} \\ \vdots \end{pmatrix}, \tag{17}$$

where $F|^{n}_{n_{\text{sg}}}$ represents all the discrete field components of the electromagnetic field F of subgrid level n_{sg} at the time instant $t = n\Delta t_{N_{\text{sg}}}$. This implies that A is a square matrix whose number of rows is equal to the total amount of field components stored in memory. In order to apply the spectral analysis explained in this section, we must consider this scheme starting from an initial time instant in which the sources are turned off (therefore we only consider finite-time sources). This also removes any other contribution to the update scheme apart from the OI-SG FDTD. This scheme is formally identical to (16) with $S|^{n} = 0\,\forall n$.

Now, for a diagonalizable operator A acting on a space of dimension d, let us consider its set of eigenvalues $\{\lambda_i\}_{i=1}^{d}$ and their respective normalized eigenvectors $\{\hat{e}_i\}_{i=1}^{d}$, which form a base. If we write the initial state expressed in terms of this base, we obtain

$$f|^{0} = \sum_{i=1}^{d} f_i\,\hat{e}_i, \tag{18}$$

where f_i is the projection of $f|^{0}$ on $\hat{e}_i$ for the given base. This allows us to express the state $f|^{n}$ at any given instant

$$f|^{n} = \sum_{i=1}^{d} f_i\,\lambda_i^{n}\,\hat{e}_i, \tag{19}$$

and it is straightforward to demonstrate that its squared norm can be written as

$$\begin{aligned} \|f|^{n}\|^{2} &= \sum_{i=1}^{d} |\lambda_i|^{2n} |f_i|^{2} + \\ &+ 2\sum_{i=1}^{d}\sum_{k=i+1}^{d} |\lambda_i|^{n} |\lambda_k|^{n} \Re\left[f_i^{*} f_k e^{jn(\theta_k-\theta_i)} (\hat{e}_i^{*}\cdot\hat{e}_k)\right], \end{aligned} \tag{20}$$

where j is the imaginary unit, * is the complex conjugate, $\Re$ represents the real part, and we have expressed the eigenvalues in polar coordinates $\lambda_i = |\lambda_i|\,e^{j\theta_i}$.

We may note that it can be bounded if we look at equation (20). Particularly,

$$\Re\left[f_i^{*} f_k e^{jn(\theta_k-\theta_i)} (\hat{e}_i^{*}\cdot\hat{e}_k)\right] \leqslant \left|f_i^{*} f_k (\hat{e}_i^{*}\cdot\hat{e}_k)\right|, \tag{21}$$

and, since d is finite, we can also define

$$B \coloneqq \max_{i,j}\left\{\left|f_i^{*} f_k (\hat{e}_i^{*}\cdot\hat{e}_k)\right|\right\}, \tag{22}$$

which does not depend on the time. This, in combination with (20) gives us

$$\|f|^{n}\|^{2} \leqslant \sum_{i=1}^{d} |\lambda_i|^{2n} |f_i|^{2} + 2B\sum_{i=1}^{d}\sum_{k=i+1}^{d} |\lambda_i|^{n} |\lambda_k|^{n}. \tag{23}$$

Now, since f_i is independent of the time and bounded by definition, it is straightforward to see that the norm diverges in the limit $n \to +\infty$ if and only if any of the eigenvalues has a norm greater than 1. Therefore, we obtain that a sufficient and necessary condition [35] to ensure non-divergence is

$$\rho\{A\} \equiv |\lambda_{\text{max}}| \leqslant 1, \tag{24}$$

where λ_{max} is the eigenvalue of A with the greatest norm, which is the well-known spectral radius of the matrix $\rho\{A\}$.

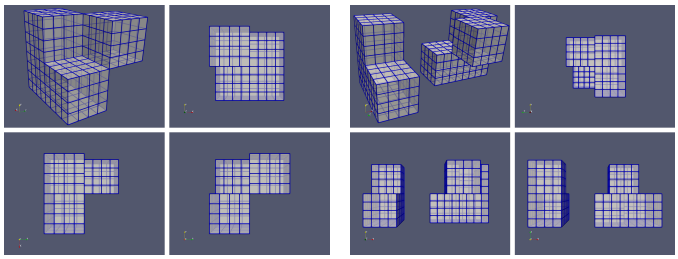

Fig. 6. Two examples of the simulation cases used for both the heuristic and spectral method. The left 2×2 set of images correspond to one simulation case and the right ones correspond to the other simulation case. For each one we show a diagonal, front, lateral and top view. We show only the finest level domain. Each coarser level wraps the current by a layer of at least one cell.

The spectral analysis has been implemented as follows. We have designed a set of simulation cases guaranteed to contain all the field types shown in Fig. 3 and Tab. I (some examples are shown in Fig. 6). All cases are designed with a maximum subgrid level of $N_{\text{sg}} = 2$, meaning a total of 3 levels. For each case, we have varied δ_{r} in the interval $[0, 1]$ with a step of 0.01; and for each value of δ_{r}, we have run simulations varying CFLN. We obtained the evolution matrix A for each resulting simulation and calculated the magnitude of its largest eigenvalue $|\lambda_{\text{max}}|$ with a numerical tolerance of 10^{-7}. Then, by using the condition derived in (24), we have obtained the largest stable CFLN.

The spectral results have also been corroborated heuristically by conducting simulations with 10^{7} iterations of the coarsest level, meaning $4{\cdot}10^{7}$ iterations of the finest one. These simulations have been performed with the same conditions as in the spectral analysis.

The results provided by the analytical formula and the spectral criterion (heuristically corroborated) are shown in Fig. 4.

IV. Locally Enlarged Cell Technique

The conclusions drawn from our analytical formula have inspired us to propose a computationally zero-cost technique to improve the CFLN condition. This section analyzes it and studies its impact on the method's accuracy.

For this, let us first introduce the basics of the LECT method and how it may be applied to improve the OI-SG. First, let us

TABLE II
LECT CONFIGURATIONS USED. WE SHOW THE VALUE OF ξ OF EACH FIELD TYPE ACCORDING TO TAB. I AND FIG. 3.

Field type	ξ (No LECT) (CFLN=0.67)	ξ (LECT-1) (CFLN=0.8)	ξ (LECT-2) (CFLN=0.9)
E-1	1.0	1.7	3.0
E-2	1.0	1.0	3.0
E-3	1.0	1.0	3.0
E-4	1.0	1.0	3.0
E-5	1.0	1.0	3.0
E-6	1.0	1.0	3.0
H-1	1.0	1.5	3.0
H-2	1.0	1.5	3.0
H-3	1.0	1.5	3.0

consider the general update equation of the FDTD method as written in (4) (this process can be analogously done with (5)), but substituting Δt with the CFL number,

$$E_i|^{n+1} = E_i|^n + \\ + \frac{\text{CFLN}}{\tilde{S}_{E,i}} \frac{\Delta}{\sqrt{3}} \sqrt{\frac{\mu}{\varepsilon}} \sum_{\substack{j \\ H_j \in \mathcal{S}\{E_i\}}} \text{sgn}_{E,i,j}\, l_{H,j}\ H_j|^{n+1/2}, \quad (25)$$

As shown in section III, for each value of δ_r, the stability depends on CFLN: the simulation is stable within a range of CFLN topped by a maximum value. In other words, if a simulation is unstable, we may stabilize it by lowering CFLN. If we take a look at (25), for a given field update, lowering the value of CFLN is equivalent to increasing its equivalent surface $\tilde{S}_{E,i}$ or lowering the surrounding edges $l_{H,j}$. This fact is a known feature of the FDTD method: larger surfaces and smaller edges are related to stability [32], [33]. We already provided an approach in (14) that implies this feature.

In the case of the OI-SG, it is interesting to note that we have already classified all the possible non-trivial fields in Tab. I by their equivalent surfaces and integration lines. Also, the analytical method described in section III-A provides information about which field pairs most likely enforce the instabilities. From this point, we may see a clear course of action that could allow us to increase the CFLN value as predicted by the model (14): artificially increase the equivalent surfaces of the most critical fields. Particularly, we define

$$\tilde{S}_{E,i,\text{new}} = \xi_{E,i}\, \tilde{S}_{E,i,\text{old}}, \quad (26)$$

where $\tilde{S}_{E,i,\text{old}}$ is the equivalent surface of the field type i as described in Tab. I, $\tilde{S}_{E,i,\text{new}}$ is the actual equivalent surface applied in the FDTD algorithm and $\xi_{E,i} \geqslant 1$ is defined as the surface-LECT parameter of the field type i. Defining a LECT parameter for the integration lines is also possible. However, we have only considered surface parameters in this work for simplicity. For all the field types described in Tab. I, we tried different LECT parameters focusing on those field components with smaller surfaces. Finally, we obtained two different configurations to test (see Tab. II): first, one that allows us to achieve CFLN $= 0.8$ (LECT-1); and second, a more aggressive one that allows us to reach CFLN $= 0.9$ (LECT-2). We compare the stability results with the non-LECT case in Fig. 7. The figure was obtained using the spectral analysis method from section III.

The described LECT-based methodology is based on increasing surfaces or decreasing lines, therefore by analyzing (10) it is immediate to verify that this method is equivalent to locally modifying the media values of ε and μ. Nonetheless, only a few fields (non-trivially updated ones) are affected, and their modification can be very slight. Also, this artificial material does not introduce numerical losses; therefore, only large LECT factors affect the precision. In addition, the LECT method does not involve modifying the OI-SG advance equations; therefore, it is zero-cost in memory and CPU usage. The impact on accuracy is illustrated in the next section.

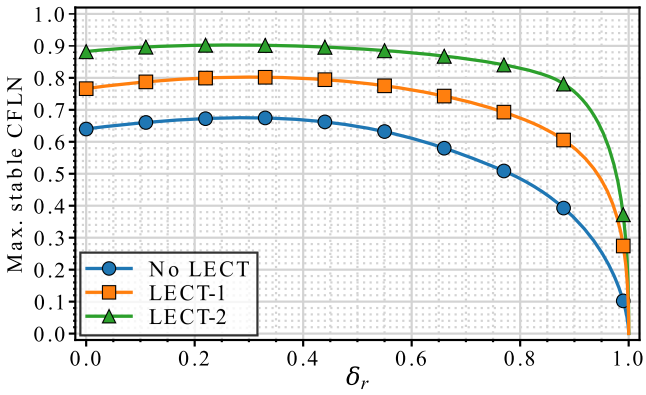

Fig. 7. Maximum stable CFLN value as a function of δ_r by the spectral analysis method for different LECT configurations. We show the original one (without LECT), one that reaches CFLN $= 0.8$ and another that reaches CFLN $= 0.9$.

V. NUMERICAL RESULTS

In this section, we intend to show the numerical accuracy and the computational performance of the LECT configurations obtained in section IV. For this purpose, we set three different simulations.

The first test case evaluates a conductive spherical shell's shielding effectiveness (SE) (ratio of the EM power in the absence of the enclosure and that when it is present). The shell is 20 mm thick and has an average radius of 1 m with an electric conductivity of 5 S/m. The sphere is illuminated with a plane wave tilted $45°$ with the x axis. The computational volume is truncated by convolutional PMLs with 10 layers [2]. The results of these simulations are shown in Fig. 8.

The second simulation evaluates the backscattering radar cross section (RCS) of a perfect electric conductor (PEC) sphere of 3 m radius. The sphere is illuminated with a plane wave with the same properties as in the SE simulation case. The numerical results of the RCS are shown in Fig. 9.

For all simulations, the finest subgridding region covers all the material parts of the space, leaving a shell of one cell between the beginning of free space and the finest subgridding boundary. For cases with more than two levels, each coarser level covers the previous one with a shell of one cell as well. The distance between the coarsest subgridding boundary and the plane wave case is 5 cells; the distance between the plane wave case and the far-field case is of another 5 cells; and the

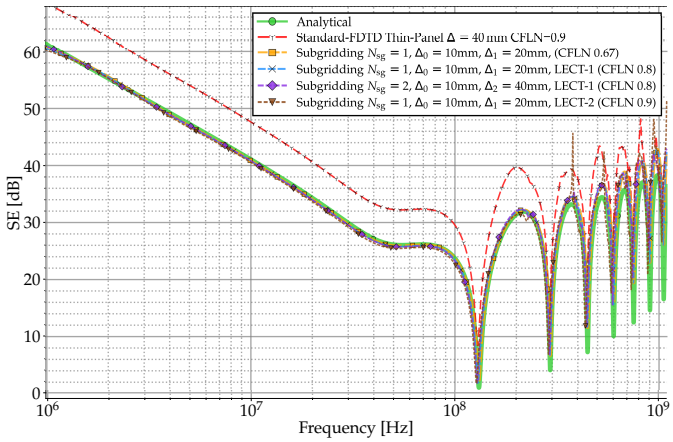

Fig. 8. Shielding Effectiveness for different LECT configurations and subgrid levels.

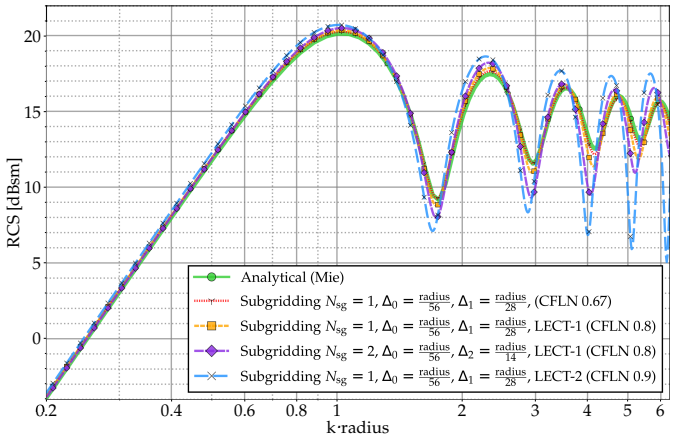

Fig. 9. Radar Cross Section for different LECT configurations and subgrid levels.

distance between the far-field case and the beginning of the PML cells is of another 5 cells (see Fig. 10).

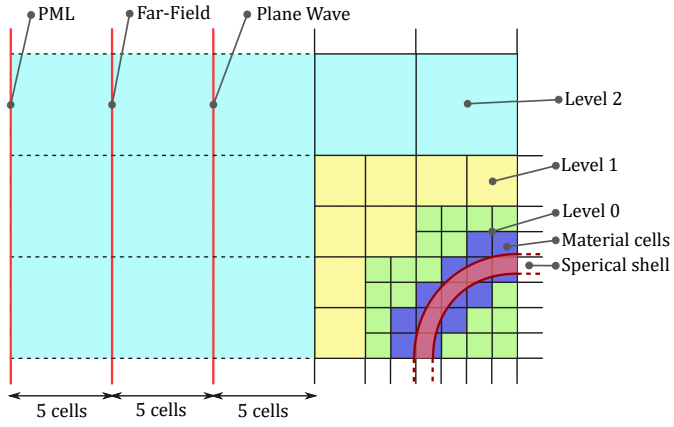

Fig. 10. Scheme of the spatial domain in the simulations performed for section V.

We also show the CPU cost and gain of the different configurations in Tab. III for the RCS simulation. In the same table, we may see that the CPU gain for the same simulation after applying LECT-1 is approximately 19.4% and an extra 12% after applying LECT-2. The table also shows the root mean square error (RMSe) for the proposed test cases, evaluated in two ranges $k \cdot \text{Radius} \in [0.2, 1.0]$ and $k \cdot \text{Radius} \in [1.0, 6.0]$.

We observe from Fig. 8 that LECT provides, in general, good agreement with OI-SG for the SE problem. However, for RCS results, we can appreciate from Fig. 9 that both LECT configurations perform less accurately than the standard OI-SG. In this case, LECT-1 outperforms LECT-2 results, as expected, since the parameters ξ used in this configuration are more aggressive (see Tab. II).

TABLE III
LECT EFFICIENCY FOR THE RCS SIMULATIONS SHOWN IN FIG. 9.

Method	N_{sg}	CFLN	Δ_{min} [m]	Δ_{max} [m]	CPU Cost	CPU Gain	RMSe in [0.2,1.0]	RMSe in [1.0,6.0]
No LECT	1	0.67	3/56	3/28	$1.056 \cdot 10^{16}$	1.000	0.168	0.202
LECT-1	1	0.80	3/56	3/28	$8.844 \cdot 10^{15}$	1.194	0.212	0.537
LECT-1	2	0.80	3/56	3/14	$5.510 \cdot 10^{15}$	1.917	0.237	1.271
LECT-2	1	0.90	3/56	3/28	$7.861 \cdot 10^{15}$	1.343	0.502	2.610

The third simulation involves a frequency-selective surface (FSS) previously simulated using a different subgridding algorithm in [36] by Xu et al. The scheme and dimensions of this simulation case are illustrated in Fig. 11. This FSS comprises an indefinitely planar PEC surface with slots of dimensions $0.02\,\text{m} \times 0.1\,\text{m}$, and these slots are periodically repeated within a unit cell of size $0.12\,\text{m} \times 0.15\,\text{m}$. Only a single unit cell is simulated to replicate an indefinite FSS, and the computational domain is truncated with periodic and absorbing boundary conditions. The boundary conditions are of the PML type [2] with 10 layers. The FSS is illuminated by a Gaussian plane wave under normal incidence, with propagation in $\hat{y}$ and polarization in $\hat{z}$, with the following waveform: $E_z(t) = \exp(-(t-t_0)^2/\tau^2)$, where $\tau = 0.23\,\text{ns}$ and $t_0 = 4\tau$. In order to study the behavior of the proposed subgridding scheme and the LECT methodology, we have evaluated the transmission coefficient shown in Fig. 12. Results found with the subgridding method proposed in this work are compared to those obtained in [36], taking as a reference the results simulated with the standard FDTD technique with a very fine grid of $\Delta_0 = 2.5\,\text{mm}$ of cell size, as well as with CST Studio Suite. It shall be noted that the refinement ratio used in [36] is 1:3 instead of 1:2. We match the cell length of level 1 in our simulations to the coarse grid in [36] ($\Delta_1 = 5\,\text{mm}$), which allows us to mimic the simulation dimensions completely and, furthermore, also to use a maximum subgridding level of $N_{sg} = 2$.

We observe that, similarly to the sphere RCS case, the LECT-1 configuration with $N_{sg} = 1$ has only a minor effect on shifting the maximum transmission frequency compared to the finest-only simulation. However, it's important to highlight that the more aggressive LECT-2 configuration significantly shifts

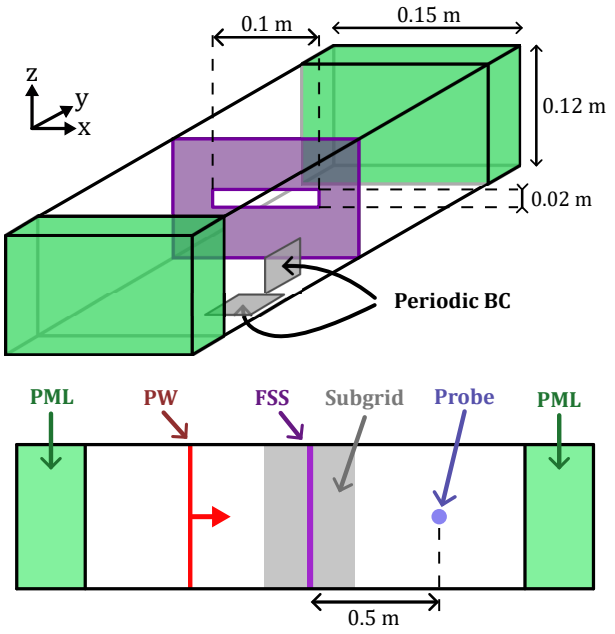

Fig. 11. Scheme of the Frequency Selective Surface from [36] that has been simulated with the OI-SG.

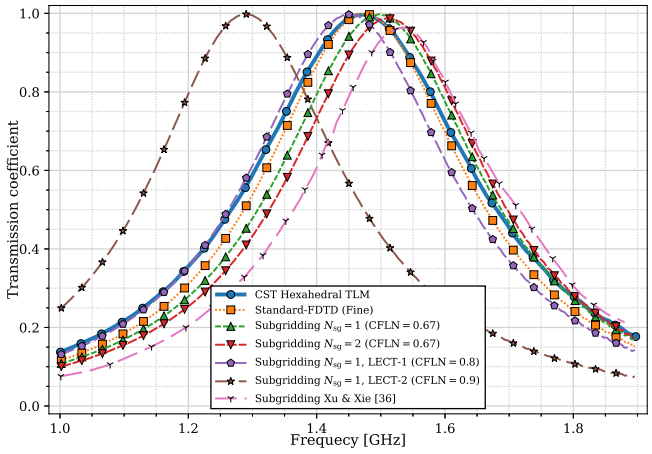

Fig. 12. Results of the simulations of the Frequency Selective Surface from [36]. All simulations have a finest level with $\Delta_0 = 2.5\,\text{mm}$ except for the simulation from [36], which has a refinement ratio of 1:3 and $\Delta_0 = 5/3\,\text{mm}$.

the maximum transmission frequency, making it unsuitable for this simulation case.

VI. Conclusions

Throughout this paper, we have used the results obtained by three different methods to study and show the necessary conditions to achieve stability of the OI-SG algorithm. Using the knowledge provided by said methods, we have located the field components that critically affect the stability. Therefore we have applied a LECT-based methodology to increase the maximum stable CFLN value from 0.67 to 0.9 with no computational cost, both memory and CPU. In addition, LECT is a non-dissipative method since the LECT corrections are equivalent to introducing lossless artificial materials. Hence for applications like SE, which evaluates an attenuation parameter through lossy materials, LECT-2 results are accurate with CPU gains of roughly 20% (CFLN = 0.9). However, RCS results, which evaluate a reflective parameter, are more sensitive to these artificial materials, and LECT-2 degrades accuracy compared to LECT-1. Generally, a trade-off must be searched between stability and accuracy on a case-by-case basis.

We must also note that the LECT-based methodology presented in this work has yet to be fully exploited. It allows us to manipulate the lengths of the integration lines, whose effects could have a different impact on the numerical results and the stability. For this reason, this is an interesting topic that can lead to future work.

Acknowledgments

The authors wish to thank Airbus DS (Getafe, Spain) for providing us with the results found with the commercial solver CST Studio Suite.

References

[1] K. Yee, "Numerical solution of initial boundary value problems involving Maxwell's equations in isotropic media," IEEE Transactions on Antennas and Propagation, vol. 14, pp. 302–307, May 1966.

[2] A. Taflove and S. C. Hagness, Computational Electrodynamics The Finite-Differences Time Domain Method. Artech House, 2005.

[3] L. C. R. P. Alessandro Vaccari, Antonino Cala Lesina, "Parallel implementation of a 3D subgridding FDTD algorithm for large simulations," Progress In Electromagnetics Research, vol. 120, pp. 263–292, 2011.

[4] F. Bekmambetova, X. Zhang, and P. Triverio, "Acceleration of shielding effectiveness analysis using stable FDTD subgridding," in 2017 IEEE 26th Conference on Electrical Performance of Electronic Packaging and Systems (EPEPS), pp. 1–3, 2017.

[5] R. Holland and L. Simpson, "Finite-difference analysis of EMP coupling to thin struts and wires," Electromagnetic Compatibility, IEEE Transactions on, vol. EMC-23, pp. 88 –97, may 1981.

[6] M. R. Cabello, L. D. Angulo, J. Alvarez, I. Flintoft, S. Bourke, J. Dawson, R. G. Martin, and S. G. Garcia, "A hybrid Crank-Nicolson FDTD subgridding boundary condition for lossy thin-layer modeling," IEEE Transactions on Microwave Theory and Techniques, vol. 65, pp. 1397–1406, Jan. 2017.

[7] M. Sarto, "A new model for the FDTD analysis of the shielding performances of thin composite structures," Electromagnetic Compatibility, IEEE Transactions on, vol. 41, pp. 298 –306, Nov. 1999.

[8] I. D. Flintoft, J. F. Dawson, L. Dawson, A. C. Marvin, J. Alvarez, and S. G. Garcia, "A modular test-suite for the validation and verification of electromagnetic solvers in electromagnetic compatibility applications," IEEE Transactions on Electromagnetic Compatibility, vol. 59, pp. 111–118, Feb. 2017.

[9] I. Kim and W. Hoefer, "A local mesh refinement algorithm for the time domain-finite difference method using Maxwell's curl equations," IEEE Transactions on Microwave Theory and Techniques, vol. 38, no. 6, pp. 812–815, 1990.

[10] P. Thoma and T. Weiland, "A consistent subgridding scheme for the Finite Difference Time Domain method," International Journal of Numerical Modelling: Electronic Networks, Devices and Fields, vol. 9, no. 5, pp. 359–374, 1996.

[11] J. Ritter and F. Arndt, "A generalized 3D subgrid technique for the finite-difference time domain method," in Microwave Symposium Digest, 1997., IEEE MTT-S International, vol. 3, pp. 1563–1566 vol.3, June 1997.

[12] F. Arndt and J. Ritter, "Advanced FD-TD techniques for the cad of 3D microwave components," Electromagnetics, vol. 23, no. 2, pp. 153–168, 2003.

[13] K. Xiao, D. J. Pommerenke, and J. L. Drewniak, "A three-dimensional FDTD subgridding method with separate spatial and temporal subgridding interfaces," in Electromagnetic Compatibility, 2005. EMC 2005. 2005 International Symposium on, vol. 2, pp. 578–583, IEEE, 2005.

[14] J.-P. Bérenger, "The Huygens subgridding for the numerical solution of the Maxwell equations," Journal of Computational Physics, vol. 230, no. 14, pp. 5635–5659, 2011.

[15] W. Tierens and D. De Zutter, "BOR-FDTD subgridding based on finite element principles," Journal of Computational Physics, vol. 230, no. 12, pp. 4519–4535, 2011.

[16] W. Tierens, "Explicit and provably stable spatiotemporal FDTD refinement," Journal of Computational Physics, vol. 375, pp. 901–917, 2018.

[17] D. M. Pederson and L. L. Raja, "A stable finite-difference time-domain scheme for local time-stepping on an adaptive mesh," Journal of Computational Physics, vol. 394, pp. 456–476, 2019.

[18] A. M. Valverde, M. R. Cabello, C. C. Sánchez, A. R. Bretones, and S. G. Garcia, "On the effect of grid orthogonalization in stability and accuracy of an FDTD subgridding method," IEEE Transactions on Antennas and Propagation, vol. 70, no. 11, pp. 10769–10776, 2022.

[19] A. M. Valverde, M. R. Cabello, A. R. Bretones, and S. G. Garcia, "An analysis of the stability of a general-purpose 3D subgridding method," IN 2022 IEEE MTT-S International Conference on Numerical Electromagnetic and Multiphysics Modeling and Optimization (NEMO), Limoges, France, 2022.

[20] P. Thoma and T. Weiland, "Numerical stability of finite difference time domain methods," IEEE Transactions on Magnetics, vol. 34, no. 5, pp. 2740–2743, 1998.

[21] A. Vaccari, R. Pontalti, C. Malacarne, and L. Cristoforetti, "A robust and efficient subgridding algorithm for finite-difference time-domain simulations of Maxwell's equations," Journal of Computational Physics, vol. 194, no. 1, pp. 117–139, 2004.

[22] T. Weiland, "A discretization method for the solution of Maxwell's equations for six-component fields," Archiv für Elektronik und Uebertragungstechnik, vol. 31, pp. 116–120, March 1977.

[23] M. Clemens and T. Weiland, "Discrete electromagnetism with the finite integration technique," Journal of Electromagnetic Waves and Applications, vol. 15, no. 1, pp. 79–80, 2001.

[24] J. Yan and D. Jiao, "Fast explicit and unconditionally stable FDTD method for electromagnetic analysis," IEEE Transactions on Microwave Theory and Techniques, vol. 65, no. 8, pp. 2698–2710, 2017.

[25] A. Van Londersele, D. De Zutter, and D. Vande Ginste, "An in-depth stability analysis of nonuniform FDTD combined with novel local implicitization techniques," Journal of Computational Physics, vol. 342, pp. 177–193, 2017.

[26] A. Van Londersele, R. Lee, F. L. Teixeira, D. De Zutter, and D. Vande Ginste, "Systematic cell-by-cell FDTD subgridding in 3-D," IEEE Microwave and Wireless Components Letters, vol. 28, no. 7, pp. 546–548, 2018.

[27] A. Van Londersele, D. De Zutter, and D. Vande Ginste, "Provably stable local application of Crank-Nicolson time integration to the FDTD method with nonuniform gridding and subgridding," in 2018 International Applied Computational Electromagnetics Society Symposium (ACES), pp. 1–2, 2018.

[28] F. Bekmambetova, X. Zhang, and P. Triverio, "A dissipation theory for three-dimensional fdtd with application to stability analysis and subgridding," IEEE Transactions on Antennas and Propagation, vol. 66, no. 12, pp. 7156–7170, 2018.

[29] Z. Ye, X. Liao, and J. Zhang, "A novel three-dimensional FDTD subgridding method for the coupling analysis of shielded cavity excited by ambient wave," IEEE Transactions on Electromagnetic Compatibility, vol. 62, no. 6, pp. 2441–2449, 2020.

[30] K. Zeng and D. Jiao, "Symmetric positive semi-definite FDTD subgridding algorithms in both space and time for accurate analysis of inhomogeneous problems," IEEE Transactions on Antennas and Propagation, vol. 68, no. 4, pp. 3047–3059, 2020.

[31] T. Xiao and Q. H. Liu, "A 3-D enlarged cell technique (ECT) for the conformal FDTD method," Antennas and Propagation, IEEE Transactions on, vol. 56, pp. 765–773, March 2008.

[32] S. Benkler, N. Chavannes, and N. Kuster, "A new 3-D conformal PEC FDTD scheme with user-defined geometric precision and derived stability criterion," Antennas and Propagation, IEEE Transactions on, vol. 54, pp. 1843–1849, June 2006.

[33] M. R. Cabello, L. D. Angulo, J. Alvarez, A. R. Bretones, G. G. Gutierrez, and S. G. Garcia, "A new efficient and stable 3D conformal FDTD," IEEE Microwave and Wireless Components Letters, vol. 26, pp. 553–555, Aug 2016.

[34] E. L. Tan and D. Y. Heh, "Stability analyses of nonuniform time-step LOD-FDTD methods for electromagnetic and thermal simulations," IEEE Journal on Multiscale and Multiphysics Computational Techniques, vol. 2, pp. 183–193, 2017.

[35] S. G. Garcia, R. G. Rubio, and A. R. Bretones, and R. G. Lopez, "Revisiting the Stability of Crank Nicolson and ADI-FDTD," IEEE Trans. on Antennas and Propagation, vol. 55, pp. 3199–3203, 2007.

[36] J. Xu and G. Xie, "A novel hybrid method of spatially filtered fdtd and subgridding technique," IEEE Access, vol. 7, pp. 85 622–85 626, 2019.